Research Article

Mechanism of In-Plane and Out-of-Plane Tribovoltaic Direct-Current Transport with a Metal/Oxide/Metal Dynamic Heterojunction

Matthew Benner, Ruizhe Yang, Leqi Lin, Maomao Liu, Huamin Li, and Jun Liu*

Cite This: *ACS Appl. Mater. Interfaces* 2022, 14, 2968−2978

Read Online

ACCESS | Metrics & More | Article Recommendations | Supporting Information

ABSTRACT: Interfacial layer engineering has been demonstrated as an effective strategy for boosting power output in semiconductor-based dynamic direct-current (DC) generators, although the underlying mechanism of power enhancement remains obscure. Here, such ambiguity has been elucidated by comparing fundamental tribovoltaic DC output characteristics of prototypical metal−oxide−metal heterojunctions prepared by atomic-layer deposition (ALD) with a vertical (out-of-plane carrier transport through the interfacial layer) and a horizontal (in-plane carrier transport along the interfacial layer) configuration such that the influences from nonequilibrium electronic excitation and interfacial capacitive amplification can be individually tuned and investigated. It is found in the case of Al/TiO$_2$/Ti vertical configurations that the open-circuit voltage (V_{OC}) increases linearly from −0.03 to −0.52 V as the thickness of titanium oxide (t_{TiO_2}) increases

from 0 to 200 nm with a linear amplification coefficient of −2.31 mV nm^{-1}, which is validated by a parallel-capacitor theoretical model with tribovoltaic electronic excitation. In contrast, the V_{OC} output with the horizontal configuration is ~55 mV, where the potential difference is merely associated with the accumulation of surface charges and the subsequent charge rearrangement in the depletion region. Meanwhile, it is measured that the short-circuit current density (J_{SC}) shows an initial increasing trend when t_{TiO_2} increases, reaches its peak value at 0.21 A m^{-2} at t_{TiO_2} = 20 nm, and then decreases as t_{TiO_2} increases further. From current−voltage ($I-V$) characterization, it is proposed that such DC output variation with an optimal interfacial layer thickness stems from the competition of amplified voltage and increased resistance with increasing interfacial layer thickness, with the main charge transport mechanism switching from quantum tunneling to thermionic emission/trap-assisted transport. In contrast, tribovoltaic excitation is proven to be significantly weaker when a wide band-gap insulator (Al$_2$O$_3$) is involved. The elucidation of the fundamental mechanism of power enhancement by the interfacial layer in this work is of great significance in providing instructional direction for the development and optimization of high-performance DC nanogenerators.

KEYWORDS: contact electrification, tribovoltaic effect, nanogenerators, dynamic DC generators, metal/oxide/metal dynamic heterojunction

INTRODUCTION

Sustainable energy solutions remain as a major challenge for miniaturized and distributed intelligent devices as the new era of internet of things has come of age.[1−3] Among green energy harvesting technologies, mechanical energy harvesting via dynamic Schottky or P−N junction-based direct-current (DC) generators is emerging as one of the most promising strategies by virtue of their exceptional advantages on high current density (J, 10−100 A m^{-2}, 3−4 orders higher than that of traditional triboelectric nanogenerators or piezoelectric nanogenerators) due to low impedance, consistent efficiency at low frequency of motion (<10 Hz), and free of power rectification.[4−7] Heretofore, considerable research efforts have been devoted to understand the mechanism of the DC generation phenomenon, as well as to explore various material schemes including 2D materials,[5,8−11] oxides,[8] perovskites,[12,13] conducting polymers,[14−18] silicon,[19−23] and liquid−semi-

conductor junctions[24,25] for enhanced DC output. Despite the large short-circuit current (I_{SC}) output, the relatively low intrinsic open-circuit voltage (V_{OC}, hundreds of millivolts) in DC generators has hindered their implementation for practical use. It is proposed that the origin of intrinsic V_{OC} generation is associated with mechanical energy-induced carrier excitation and the resulting Fermi energy misalignment, which is analogous with photovoltage generation in solar cells and thus has been referred to as the "tribovoltaic" effect.[3,26−28] In addition, the existence of interfacial layers, adsorption, image

Figure 1. (a) Schematic demonstration of TiO$_2$ thin-film deposition via ALD; AFM topographic image of the (b) 10 nm and (c) 100 nm TiO$_2$ surface. Schematic diagram of the Al/TiO$_2$/Ti dynamic DC generator with (d) vertical configuration employing both the intrinsic and capacitive effects and (e) horizontal (in-plane) configuration employing only intrinsic effect for DC power generation. Red arrows indicate the direction of electron transfer; energy band diagrams under short-circuit conditions with (f) a thin TiO$_2$ (tens of nanometers) as the interfacial layer, where direct tunneling dominates the contribution to the DC generation along with a limited amount of Fowler–Nordheim (F–N) tunneling and thermionic emission, corresponding to the transport of mechanoelectronically excited carriers with relatively low, moderate, and high energy, respectively; (g) thick TiO$_2$ (>70 nm) as the interfacial layer in vertical configuration or for horizontal configuration (t_{oxide} = infinite), where trap-assisted injection and/or thermionic emission is responsible for charge transfer across the Schottky barrier, as indicated by the I–V results (Figure 4).

charges, and surface-/geometry-sensitive electromechanical coupling (e.g., surface piezoelectricity or flexoelectricity) at physical contacts may introduce additional implications to the overall voltage output. As for the DC charge transport mechanism, different physical pictures (e.g., quantum tunneling,[20] thermionic emission,[1,29] defect-assisted transmission,[8] and interfacial reflection[22]) have been proposed without an explicit consideration of the energy distribution of carriers and interfacial conditions.

In order to optimize the DC output level of dynamic DC generators, introducing a thin interfacial layer (<1 μm) at the metal–semiconductor or PN junction insertion approach has been proven to be an effective approach.[6,8,20,30,31] By inserting a layer of different kind of dielectric materials (i.e., AlN, SiO$_2$, Al$_2$O$_3$, ZnO, and HfO$_2$) into dynamic PN junctions via physical vapor deposition, Lu et al.[32] found that the enhanced V_{OC} shows a good accordance with the theoretical barrier height of the heterojunction formed by the contact metal and interfacial dielectric material.[9,32] Among the dielectric interfacial materials being tested, AlN exhibits the largest barrier height (5.3 eV) in MoS$_2$/AlN/Si sliding contact and a maximum V_{OC} output of ~5.0 V. It was measured that the V_{OC} increases from ~0.7 to ~4.0 V, and the I_{SC} decreases from 1.8 to 0.3 μA (the corresponding current density, J_{SC}, drops from 1.80 to 0.26 A m^{-2}) when the SiO$_2$ thickness is increased from 0 to 200 nm.[9,32] The boosted V_{OC} is attributed to the enhanced barrier height and more energetic hot carriers being

charged and discharged at the interface of two contacting materials. However, the actual barrier height of these physically contacted systems has not been experimentally validated, and the contribution of thermionic emission and defect-assisted carrier transport cannot be ruled out. A quantum-tunneling charge-transfer model for DC generation has been proposed by Liu et al.[20] in a metal/SiO$_x$/silicon (Si) DC generator, reporting that the V_{OC} increases from 0.5 to 3 V, whereas the J_{SC} decreases exponentially from ~2 to ~0 A m^{-2} when the atomic layer deposition (ALD)-prepared oxide thickness increases from 0 to 10 nm. However, a different tendency of J_{SC} has been observed in the case of MoS$_2$/TiO$_2$/Ti moving contacts with electron-beam (E-beam)-evaporated TiO$_2$ as the interfacial layer, where an optimal V_{OC} (0.7 V) and J_{SC} output (1.2 A m^{-2}) has been found at a TiO$_2$ thickness of 60 nm.[8] It is proposed that the TiO$_2$ film evaporated by the E-beam may contain electrically conductive pathways (defects, grain boundaries, etc.), allowing the frictionally excited charge carrier to thermionically get across the interfacial barrier and being conductive through it rather than by quantum tunneling.[33] However, there was a lack of experimental evidence supporting the theory. It is also proposed that a larger interfacial charge accumulation (Δσ) and thus an enhanced V_{OC} output may be expected due to the capacitive amplification in the oxide thickness range of 0–60 nm. However, further increasing the thickness of the dielectric layer may result in a smaller Δσ according to the double-capacitor

model.[34] In the meantime, a thicker dielectric layer increases the internal resistance of the generator, resulting in a decreased current output. Another evidence of the interfacial layer influence is the reverse and recovery of DC output polarity when the oxide of Si is first etched by hydrofluoric acid and regrows.[30] Nevertheless, all of these material systems inevitably involve both intrinsic (tribovoltaic carrier excitation) and capacitive amplification effects. As a result, multiple capacitors, including the interfacial gap (physical contact interface, 0.1−1 nm), interfacial dielectric layer, and surface charge region (SCR), are connected in series in the equivalent circuit model of metal (semiconductor)−insulator−semiconductor physical contacts, complicating the physical mechanism of DC generation. Moreover, the morphological and electrical properties of the interfacial layer can impact the DC current generation. Therefore, there is a pressing need to reveal the fundamental mechanism by deconvoluting the contribution of these factors in an effort to provide an instructional guide for the optimization of DC generators.

Herein, fundamental roles of the interfacial dielectric layer on the voltage output enhancement and DC transport mechanism have been elucidated. In order to reveal the contribution of Fermi-level misalignment due to tribovoltaic carrier excitation and the capacitive effects of the insulating layer, prototypical metal−insulator−metal (MIM) sliding heterojunctions with horizontal (in-plane) and vertical (out-of-plane through the interface) DC transport pathways were designed and fabricated by thickness-controlled ALD of titanium dioxide (TiO_2) and alumina (Al_2O_3). Comparisons of intrinsic and oxide thickness t_{oxide}-dependent DC power output along with interfacial electronic characteristics have been conducted to facilitate the quantitative formulation of interfacial layer-enhanced tribovoltaic carrier excitation and transport. The fundamental understanding of nonequilibrium electronic excitation at the sliding heterojunction is the key for improving the mechanical energy harvesting performance of future dynamic DC generators, which may also lead to novel multiphysics interaction with enhanced efficiency.

■ EXPERIMENTAL SECTION

Titanium (Ti) and Aluminum (Al) Thin-Film Deposition. E-beam evaporation was employed to deposit the Ti and Al thin film onto a glass substrate [E-beam evaporator with glancing angle deposition (GLAD) from Kurt J. Lesker Company AXXIS]. All samples had 50 nm of titanium/aluminum deposited on an ethanol-prerinsed glass substrate. Ti pellets (purity: 99.995%) and Al pellets (purity: 99.999%) were purchased from Kurt J. Lesker Company as evaporation targets. Before the deposition, the system was pumped down to a pressure of $<10^{-6}$ Torr with 500 mA beam sweep. The top rotating plate was spinning at a rate of 20 rpm, and the target deposition rate was set as 0.8 Å s^{-1} during deposition. The deposited thickness was supervised by two quartz crystal microbalance thickness monitors.

TiO_2 and Al_2O_3 Thin-Film Deposition. ALD was used to deposit the TiO_2 and Al_2O_3 thin films. As one of the most recognized deposition methods, ALD has been known for its high-level deposition quality (exceptional uniformity of deposition with controlled defect). The ALD process works as shown in Figure 1a. The precursors used for TiO_2 deposition were tetrakis-(dimethylamido)titanium, $Ti(NMe_2)_4$ (TDMAT) and pure distilled water (H_2O). Trimethylaluminum (TMA) and pure distilled water were used to deposit Al_2O_3 thin films (the TDMAT and TMA precursors were purchased from STREM Chemical Company). The system was heated to a temperature of 150 °C for TiO_2 deposition and 80 °C for Al_2O_3 deposition. After each recipe step, the system was

purged with nitrogen (N_2) at a flow rate of 90 sccm. The deposition rate at 150 °C was 0.80 Å per cycle for TiO_2 and 1.07 Å per cycle at 80 °C for Al_2O_3. Therefore, the desired thickness was controlled by setting the necessary cycle number.

For the vertical devices, a 50 nm Ti/Al thin layer was deposited onto glass substrates for all samples via the E-beam evaporator. Then, the samples were transferred into the ALD chamber for TiO_2 (5, 10, 20, 30, 70, 100, and 200 nm) and Al_2O_3 (1, 3, 5, and 10 nm) depositions with 30% of each sample area covered by a hard mask. The hard-masked region was designed to a complete circuit for later DC power and $I-V$ measurements. For the horizontal devices, a 50 nm ALD-deposited TiO_2 thin film was initially prepared onto glass substrates, followed by another 50 nm Ti deposition inside the E-beam vacuum chamber. Similar to the vertical devices, a hard mask was used to set up a region for completing the circuit.

Atomic Force Microscopy Characterization. Atomic force microscopy (AFM) characterization was conducted using a Bruker Icon AFM (Santa Barbara, CA) system. In the AFM experiment, the peak force tapping mode was used to obtain the topographic information of the ALD-deposited thin films. An electrically conducting AFM probe (Pt-/Ir-coated, ANSCM-PT, AppNano) with a resonance frequency of 60 kHz, a spring constant of 3 N m^{-1}, and a tip of radius of curvature of 30 nm was used as the probe. Multiple locations on the ALD-prepared thin film were tested with a scan size of $\sim 1 \times 1$ μm. The topographic images were processed, and the surface roughness was analyzed using NanoScope Analysis software (V2.0, Bruker).

Triboelectric DC Power Characterization. The triboelectric DC characterization was performed with a customized electromechanical testing system. For the sample characterization, an Al probe (contact area $A \approx 4$ mm^2) was fixed to a static force gauge (Torbal Scientific Industries Inc., part number: FB-5) and the samples were fixed to a platform connected to a linear actuator (Fourien Inc., part number: LA-5039). The speed of the actuator was controlled to be 15 mm s^{-1}, and the force between the contact and the samples was controlled to be approximately 0.10 N. In force-dependent measurement, the power generation was performed under 0.05, 0.10, 0.15, and 0.20 N (within 10% deviation) and a constant velocity (15 mm s^{-1}). For the velocity-dependent experiment, the power generation was performed under 5, 10, 15, 20, and 25 mm s^{-1} and a constant force (0.10 N). The electrical output data was collected using a Keithley DM6500 digital multimeter, and the force data was simultaneously recorded by the force gauge. For the $I-V$ curves, a Keithley 2450 Interactive source meter was used to provide the biased voltage and measure the current output. The sweep range was set from −5.0 to 5.0 V. The step and sampling rate were set as 10 mV and 1 Hz, respectively.

■ RESULTS AND DISCUSSION

In order to distinguish the intrinsic effects (i.e., tribovoltaic effect) of metal−insulator contact and the capacitive effects of the insulating layer on the DC power output, two different configurations of MIM samples were fabricated with the aid of ALD, as shown in Figure 1a. A vertical configuration is shown in Figure 1d with an increasing thickness of TiO_2 (5, 10, 20, 30, 70, 100, and 200 nm) as the interfacial layer deposited on a glass substrate with a predeposited Ti (50 nm) layer. As shown in Figure 1b,c, the root-mean-square surface roughness (R_q) of the as-prepared sample was measured to be 0.9 and 1 nm for the 10 nm and 100 nm thin films, respectively (see Figure S1 in the Supporting Information for more AFM results). On the other hand, as shown in Figure S2, the average R_q for the cross-sectional surface of Al probes was measured to be 6.81 nm (Table S1). A horizontal configuration is shown in Figure 1e with a 50 nm Ti layer deposited on a glass substrate with a 50 nm predeposited TiO_2 layer.
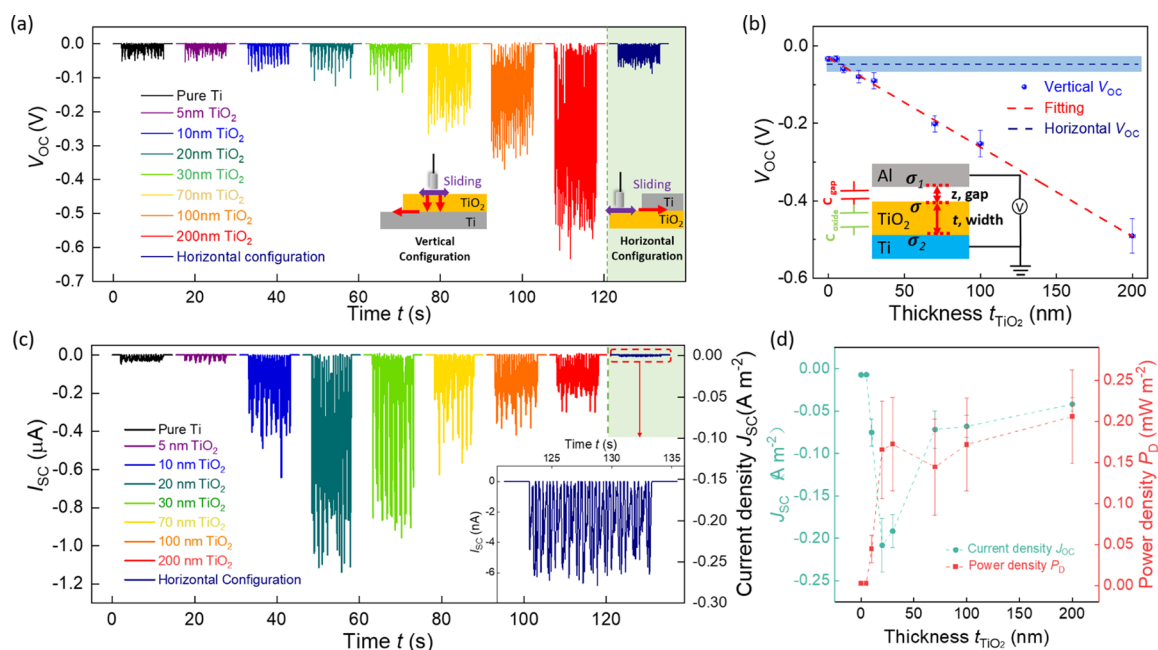
Figure 2. (a) Comparison of the V_{OC} output between the vertical structure with an increasing TiO$_2$ thickness (t_{TiO_2} = 0, 5, 10, 20, 30, 70, 100, and 200 nm) and the horizontal structure (t_{TiO_2} = 50 nm); (b) linear fitting result of the collected V_{OC} output of the vertical structure with an increasing TiO$_2$ thickness t_{TiO_2} = 0, 5, 10, 20, 30, 70, 100, and 200 nm; inset: schematic illustration of the contact electrification process by the metal−oxide−metal system (Al/TiO$_2$/Ti); (c) comparison of the I_{SC} and J_{SC} (4 mm^2 contact area) output between the vertical structure with an increasing TiO$_2$ thickness (t_{TiO_2} = 0, 5, 10, 20, 30, 70, 100, and 200 nm) and the horizontal structures (t_{TiO_2} = 50 nm); (d) average J_{SC} and theoretical power output P_D as a function of the thickness of the TiO$_2$ layer.
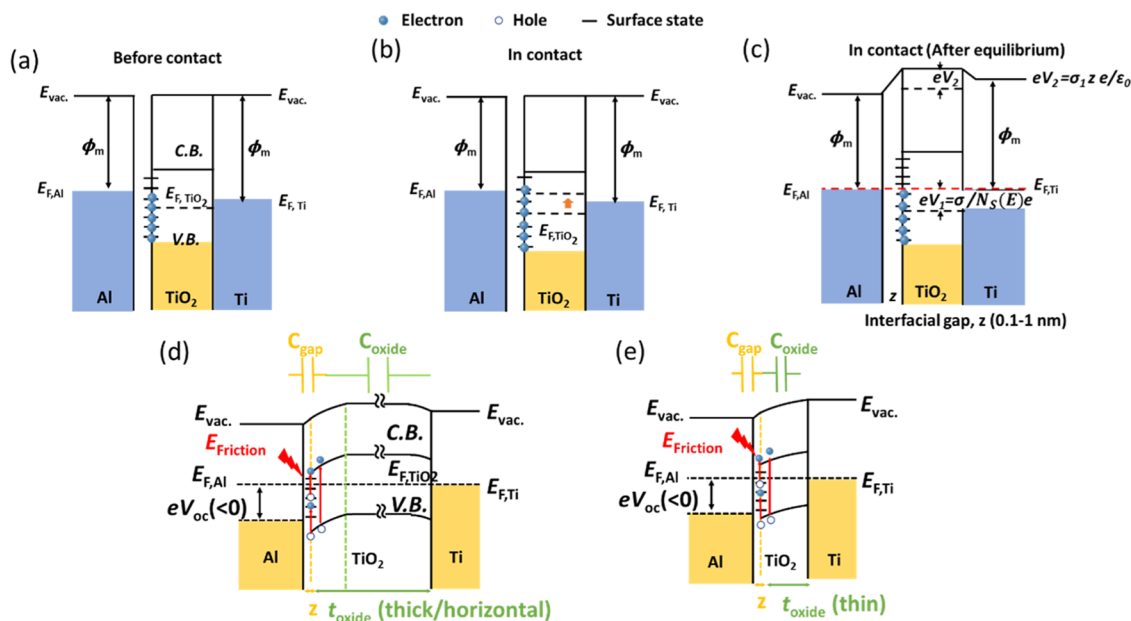
Figure 3. Simplistic model (without considering band bending) of energy band diagram for the metal and dielectric material (a) before contact, (b) in contact with no bias, and (c) separation equilibrium with no bias (interfacial gap z typically under or around the order of 1 nm); energy band diagrams under open-circuit conditions with (d) thick TiO$_2$ (>70 nm) as the interfacial layer in a vertical configuration or for all horizontal configuration and (e) thin TiO$_2$ (tens of nanometers) as the interfacial layer, where electronic excitation may lead to (1) excited valence electrons from the valence band to the conduction band (band-to-band excitation); (2) excited surface electrons from surface states to the conduction band (sub-band-gap excitation), or (3) excited valence electrons from the valence band to surface states (sub-band-gap excitation).

Figure 1f,g shows the short-circuit energy band diagrams of the contacting metal−semiconductor with an interfacial gap (z) between a thin TiO$_2$ (tens of nanometers, Figure 1f) or a thick TiO$_2$ >70 nm (Figure 1g) and the contact metal. Such

gap is the result of physical contact between the probe and the thin film, which is in the range of 0.1−1 nm. The capacitive effect could be summarized as a gap-induced capacitor (C_{gap}) combined with an oxide layer-induced capacitor (C_{oxide}). It

should be noted that C_{oxide} includes the capacitance of the bulk film and the SCR between metals and the oxide layer [(a) between Al and oxide layer; (b) between the oxide layer and Ti]. Figure 1f also shows the transfer of excited holes in the vertical configurations with a thin layer of TiO_2 (tens of nanometers). Specifically, excited holes with relatively low, moderate, and high energy are transmitted from Al to Ti by direct quantum tunneling, F−N tunneling[35−37] (through the triangular-shaped barrier), and thermionic emission (across the Schottky barrier),[38,39] respectively. It is believed that such energetic "hot" tribovoltaic carriers may follow a Boltzmann distribution.[40] Therefore, direct tunneling may dominate the carrier-transfer process, accompanied by F−N tunneling thermionic emission with less probability. In the case of vertical configuration with a thicker TiO_2 interfacial layer (>70 nm as indicated later in the $I−V$ results), it is proposed that tribovoltaic carriers (holes in this case) are excited by the frictional energy exerted at the Al/TiO_2 sliding interface, transmit across the interfacial energy barrier (Schottky barrier) via thermionic emission/trap-assisted transport, and get swept by the built-in electric field in the SCR (Figure 1g). The existence of the interfacial dielectric layer can induce a capacitive voltage amplification, which will be discussed in detail later. For a horizontal configuration (Figure 1e), such capacitive amplification effect can be neglected.

Figure 2a,c shows the time-dependent V_{OC} and I_{SC} output of the vertical configuration (schematic illustration shown in left inset figure) with varying thickness of TiO_2 (t_{TiO_2} = 0, 5, 10, 20, 30, 70, 100, and 200 nm) and horizontal configuration with 50 nm TiO_2 (schematic illustration shown in the right inset figure), respectively. The thickness-dependent V_{OC} and J_{SC}, theoretical power density output, are summarized in Figure 2b,d, respectively. In Figure 2a, an increase of V_{OC} from −0.03 to −0.52 V can be observed as the thickness of the TiO_2 layer increases from 0 to 200 nm. The negative polarity of the V_{OC} output is due to the downward banding and its corresponding direction of the built-in electric field in TiO_2 (from Al to TiO_2; holes transmit from Al to TiO_2). The frequency of the signal spike coincides with the frequency of the sample movement driven by the linear motor system, while the normal force and velocity will impact the amplitude of the spikes. It is worth to point out that the pure Ti also exhibits energy output which could be attributed to the existence of the native oxide layer on the metal surface (3−7 nm).[41]

In the vertical configuration, the DC voltage generation can be ascribed to the result of both intrinsic (triboelectrification between Al and TiO_2) and capacitive (due to the dielectric behavior of TiO_2) effect. In contrast, only the intrinsic effect is involved in the DC voltage generation in the horizontal configuration. Accordingly, a model presented by Zhou et al.[34] was applied to examine the capacitive effects. In this model, parallel-plate assumptions for capacitors are employed. Figure 3a−c shows the simplified energy band diagrams of the model (without considering the surface band bending). The highest filling surface energy state of the dielectric material is lower than the Fermi level of the metal, as shown in Figure 3a. When the metals and the oxide come in contact, the electrons in the metal will flow from the top metal electrode to the surface of the dielectric to fill the surface state as high as the Fermi level of the metal (Figure 3b). Due to this locally established potential, part of the charge on the surface of the dielectric can

flow back to the metal.[42,43] According to this model, the state charge neutrality can be stated as[34]

$$\sigma + \sigma_1 + \sigma_2 = 0 \tag{1}$$

where σ, σ_1, and σ_2 represent the charge density on the dielectric surface, top electrode surface, and bottom electrode surface, respectively. As the dielectric layer and top electrode are separated from each other, there is an induced electric field due to the transferred charge on the dielectric surface and the image charge on the top electrode (Figure 3c). The built-in electric field, ΔE_{vac}, can be modeled as[34]

$$\Delta E_{vac} = \frac{\sigma_1 z e}{\varepsilon_0} \tag{2}$$

where z is the effective interface distance between the physically contacted top electrode and dielectric surface, which is usually in the range of several angstroms. When the system is in equilibrium, the dielectric surface states will be filled as high as the Fermi energy level and the charge on the dielectric can be molded as seen in eq 3. Likewise, the average surface state density can be modeled as seen in eq 4[34,44]

$$\sigma = -e \int_{E_0}^{E_0 + \Delta E_s} N_s(E) dE \tag{3}$$

$$N_s(E)_{avg} = \frac{\int_{E_0}^{E_0 + \Delta E_s} N_s(E) dE}{\Delta E_s} \tag{4}$$

where E_0 is the surface work function of the dielectric and $N_s(E)$ is the surface density of state. From eqs 3 and 4, the total energy range of the filled surface state can be modeled as seen in eq 5.[34]

$$\Delta E_s = -\frac{\sigma}{N_s(E)_{avg} e} \tag{5}$$

By combining eqs 1−5, the work function difference of the dielectric and the top electrode can be expressed as eq 6.[34]

$$E_0 - W = \Delta E_{vac} + \Delta E_s = \frac{\sigma_1 z e}{\varepsilon_o} - \frac{\sigma}{N_s(E)_{avg} e} \tag{6}$$

where W is the work function of the top electrode. Looking at the voltage difference between the two electrodes (again operating under the parallel-plate assumptions), the measured voltage difference can be expressed as seen in eq 7[34]

$$V = \frac{\sigma_1 z}{\varepsilon_0} - \frac{\sigma_2 t_{oxide}}{\varepsilon \varepsilon_o} \tag{7}$$

where t_{oxide} is the thickness of the oxide dielectric layer. Analyzing the model of Zhou et al.[34] along with the above equations, eq 8 can be further derived

$$\sigma = \frac{V + \left(\frac{W - E_0}{e}\right)\left(1 + \frac{t_{oxide}}{\varepsilon z}\right)}{\frac{t}{\varepsilon \varepsilon_o} + \left(\frac{1}{N_s(E)_{avg} e^2}\right)\left(1 + \frac{t}{\varepsilon t_{oxide}}\right)} \tag{8}$$

Rearranging eq 8 to solve the potential difference

$$\Delta V = \left(\frac{1}{\Delta z}\left(\frac{\Delta \sigma}{\varepsilon}\left(\frac{\Delta z}{\varepsilon_0} + b\right) - \frac{a}{\varepsilon}\right)\right) t_{oxide} + (\Delta \sigma b - a) \tag{9}$$

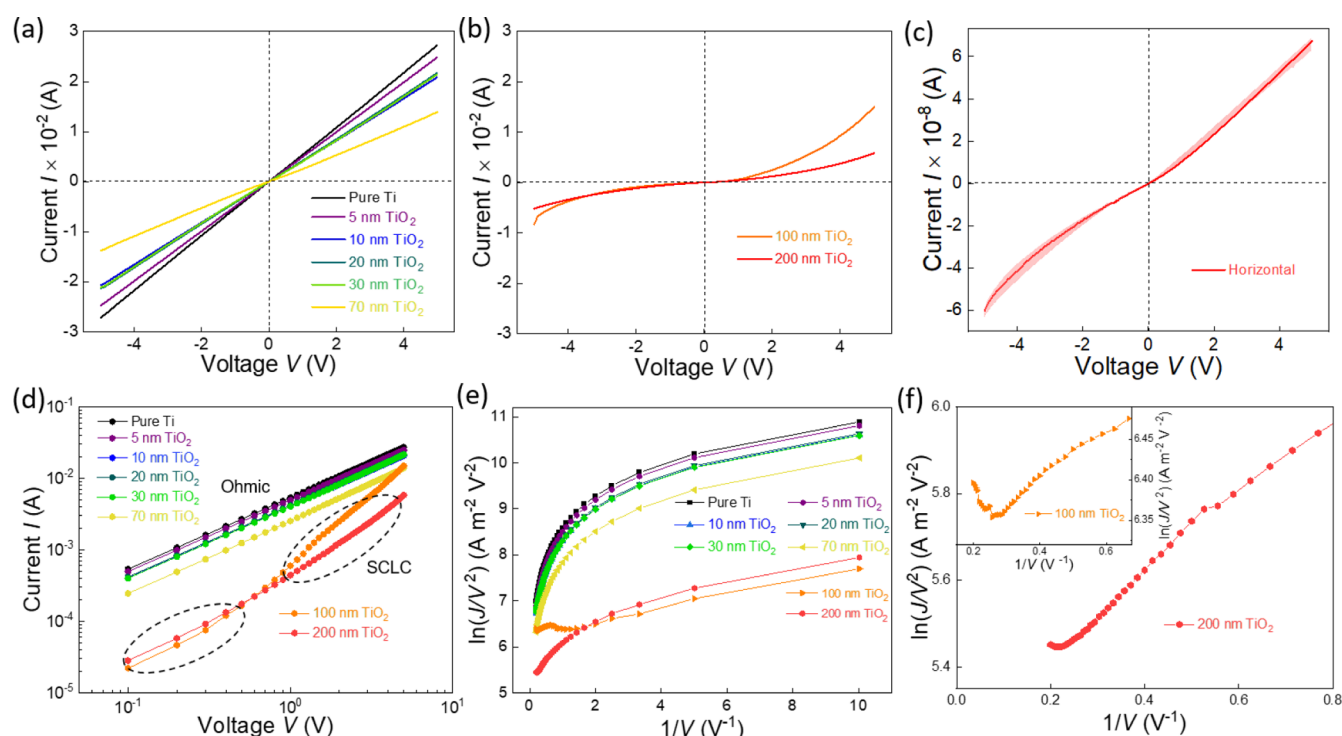**Figure 4.** I−V characterizations of (a) vertical configuration with t_{TiO_2} = 0, 5, 10, 20, 30, and 70 nm (b) vertical configuration with t_{TiO_2} = 100 and 200 nm, which displays the increase in resistance as the thickness of the TiO_2 layer increases and the transition from Ohmic to Schottky contact feature; (c) I−V characterizations of the horizontal configuration with t_{TiO_2} = 50 nm; error band area represents the standard deviation; (d) logarithmic I−V characterizations of vertical configuration with t_{TiO_2} = 0, 5, 10, 20, 30, 70, 100, and 200 nm; notably, a space-charge limited-current (SLSC) mechanism is inferred when t_{TiO_2} reaches 100 nm; (e) I−V characteristics of the vertical configuration with t_{TiO_2} = 0, 5, 10, 20, 30, 70, 100, and 200 nm based on the F−N tunneling model, $\ln(J/V2)$ vs $1/V$ curves; (f) zoomed-in view of the $\ln(J/V^2)$ vs $1/V$ curve of 200 nm TiO_2 shows the trough region; inset: zoomed-in view of the $\ln(J/V^2)$ vs $1/V$ curve of 100 nm TiO_2.

where $a = \frac{W - E_0}{e}$ and $b = \frac{1}{N(E)e^2}$. The quantities "a" and "b" are treated as constants for systems made of the same materials. When the heterojunction is subjected to friction without any bias voltage being applied to the heterojunction, the potential difference ΔV becomes the open-circuit voltage V_{OC}. Herein, we assume the change in the interfacial distance Δz to be constant due to the fact that the fluctuation of contact force is less than 10% during friction. Lastly, the change in the surface charge density of the dielectric $\Delta \sigma$ is also taken as a constant.[34] From the above assumptions, eq 9 can be reduced to the following

$$\Delta V = V_{oc} = c t_{oxide} + d \qquad (10)$$

where $c = \frac{1}{\Delta z}\left(\frac{\Delta \sigma}{\varepsilon}\left(\frac{\Delta z}{\varepsilon_0} + b\right) - \frac{a}{\varepsilon}\right)$, $d = (\Delta \sigma b - a)$, $a = \frac{W - E_0}{e}$, and $b = \frac{1}{N(E)e^2}$. Equation 10 indicates that V_{OC} should vary linearly with the thickness, which is in good accordance with the experimental results as shown in Figure 2b: the linear fitting result of average V_{OC} with the vertical structures as a function of t_{TiO_2}. The inset figure shows the schematic illustration of the parallel model of the Al/TiO_2/Ti junction with a vertical configuration. A linear coefficient of −2.31 mV nm^{-1} and a y-intercept of −30.55 mV are observed, which are in good accordance with eq 10. It can be inferred from eq 10 that such a linear coefficient is associated with the dielectric constant and surface state density of the interfacial material. As a comparison, the V_{OC} obtained in the horizontal configuration

remains around −55 mV, which corresponds to the intrinsic voltage output without any influence from the capacitive amplification effect. Here, it is worth mentioning that with a horizontal configuration, the current should transfer along the surface of TiO_2 layer instead of passing through the TiO_2 thickness due to the orders-of-magnitude difference in the electrical resistance between TiO_2 and Ti. It can be seen that the intrinsic V_{OC} output is close to the output under vertical configuration (−59 mV) with a less oxide thickness (<10 nm).

As for the mechanoelectronic excitation, it is proposed that energetic carriers can be induced by frictional energy exerted at the sliding interfaces, which is also referred to as the "tribovoltaic" effect.[28,30,45,46] Such electronic excitation may lead to (1) excited valence electrons from the valence band to the conduction band (band-to-band transition), (2) excited surface electrons from the surface states to the conduction band (sub-band-gap transition), or (3) excited valence electrons from the valence band to the surface states (sub-band-gap transition) (Figure 3d,e). It is noted that the excited charges trapped at the surface states may interact with bulk trap states as well, which will be shown in the I−V results later. As a result, a potential difference related to the difference in the Fermi levels of the contacting Al tip and TiO_2 layer is created. In the vertical configuration, the power generation could be ascribed to a result of both intrinsic effect and capacitive effect, where the latter effect could be amplified by the interfacial layer thickness, resulting in V_{OC} enhancement.

The I_{SC} and its corresponding current density J_{SC} have also been measured for both vertical and horizontal configuration.
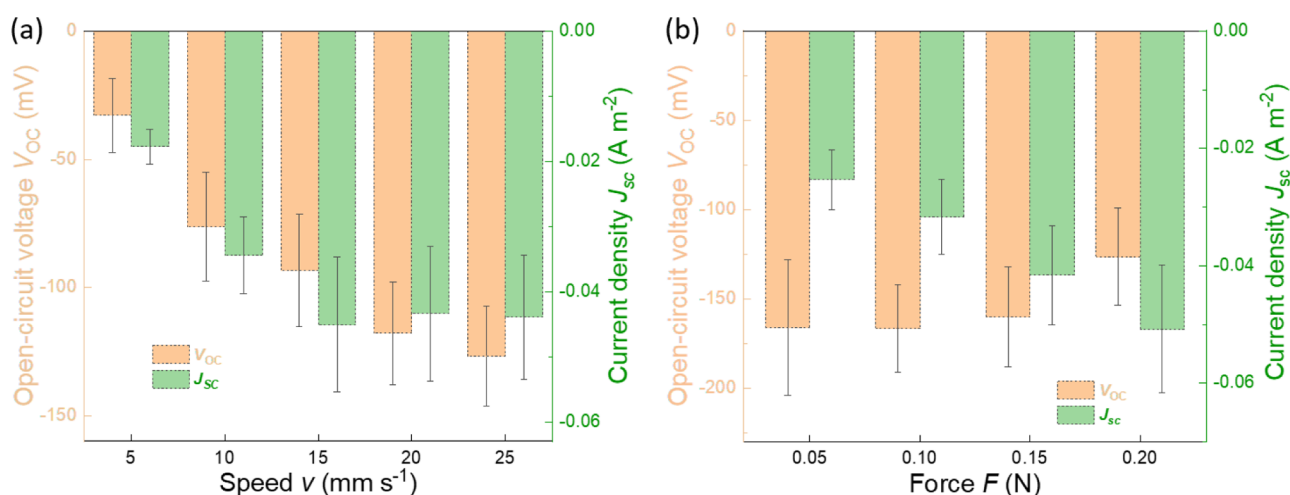
Figure 5. (a) Speed-dependent V_{OC} and J_{SC} output, both showing a positive correlation with increasing sliding speed (5−25 mm s^{-1}); (b) force-dependent V_{OC} and J_{SC} outputs showing a positive correlation with increasing enlarging applied force F (0.05−0.2 N).

As shown in Figure 2c, it can be seen that the I_{SC} (J_{SC}) output as a function of time at different oxide thicknesses increases from −0.02 μA (0.007 A m^{-2}) to −0.22 μA (0.04 A m^{-2}) when the oxide thickness increases from 0 to 200 nm, peaks around 20 nm with a maximum current output of −1.13 μA (0.21 A m^{-2}), and then decreases. As for the in-plane structure, it can be seen that the I_{SC} (~6 nA) is much lower than what can be achieved from the vertical-layer structure. Figure 2d summarizes the average J_{SC} and theoretical power density, P_D output (product of J_{SC} and V_{OC}) of the vertical structures versus the thickness of the TiO$_2$. The theoretical power increases quickly from 0.002 to 0.17 mW m^{-2} when the thickness of the TiO$_2$ layer increases from 0 to 30 nm and then increases slowly to 0.21 mW m^{-2} as the thickness increases further to 200 nm.

In order to further explain the different tendency of J_{SC} versus t_{TiO_2} compared to that of V_{OC} versus t_{oxide}, $I-V$ characterizations of both vertical and horizontal configurations have been conducted to reveal their interfacial electronic structure. Figure 4a shows the $I-V$ characterization measurements of each vertical configuration samples with t_{TiO_2} increasing from 0 to 70 nm. All the $I-V$ curves in Figure 4a show a clear linear feature, which indicates an ideal Ohmic contact forms at the Al and TiO$_2$ interface when $t_{TiO_2} \leq 70$ nm, suggesting the formation of Ohmic contact. On the other hand, the $I-V$ characterizations at a higher thickness ($t_{TiO_2} = 100$ and 200 nm) in Figure 4b exhibit a distinct nonlinear feature, which is an indication of Schottky contact formation between the Al and the TiO$_2$ layer with an emerging interfacial energy barrier height and a built-in electric field due to surface band bending (Figure 1g). From the variation of the current level in $I-V$ curves, it can also be seen that the resistance increases as the oxide layer increases. Accordingly, the observation of first increasing and then decreasing J_{SC} versus oxide thickness as shown in Figure 2d can be ascribed to the competition of increasing voltage and the increasing resistance resulting from the increasing oxide thickness.[47] It is also worth mentioning that the ionic passivation of ultrathin TiO$_2$ (<20 nm) may also facilitate current transfer through the interface.[48,49] Additionally, the horizontal configuration of $I-V$ characterizations presents 6 orders of magnitude lower than the vertical

configuration in terms of current (Figure 4c), which is ascribed to the much larger resistance of the TiO$_2$ surface in the in-plane carrier transport configuration and can be used to explain the much lower J_{SC} output demonstration.

It is hypothesized that the energy of friction-induced hot carriers in the 2D van der Waals heterojunction may follow a Boltzmann distribution as indicated by the DC output as a function of barrier height[40]

$$\Delta\sigma(E) \propto \exp(\varphi_B/kT_{eff}) \qquad (11)$$

where k is the Boltzmann constant and T_{eff} is the effective temperature at the sliding interface (local temperature at single asperity can be as high as 1000 K). Therefore, tunneling-based mechanisms would dominate the charge transport when the oxide is thin (tens of nanometers), whereas thermionic emission/trap-assisted transport becomes the major mechanism when the oxide is thicker (>70 nm) as the tunneling probability decreases exponentially versus dielectric thickness.

To further testify the above hypothesis, logarithmic $I-V$ curves have been analyzed, as shown in Figure 4d. It can be seen that a linear Ohmic transport appeared for TiO$_2$ with thickness <70 nm. On the contrary, two distinguished regions can be observed in the $I-V$ curve (marked with dashed lines) when the thickness of TiO$_2$ is 100 and 200 nm, indicating a transition from the valence-band hole transport at the voltage < ~0.4 V to trap-limited SLSC as the voltage further increases.[33,50] Therefore, it is inferred that trap-assisted SLSC also contributes to the tribovoltaic DC transport with a relatively thicker oxide layer. Additionally, by plotting $\ln(J/V^2)$ versus $1/V$ curves as shown in Figure 4d,e, no trough region is found for horizontal (Figure S3d) and vertical TiO$_2$ with low thickness (<70 nm) (Figure 4e), which means that F−N tunneling is not involved under these conditions. Under these oxide thicknesses, direct tunneling should be responsible for the charge transfer, which is understandable due to the low thickness of the interfacial layer (the local thickness could be even lower than the as-deposited thickness because of the indentation from the moving metal probe). Additionally, the band bending should be more influenced by the work function difference between Al and Ti, which makes the bending relatively mild and results in a much narrower triangular area for F−N tunneling to take place. With a zoomed-in plot of
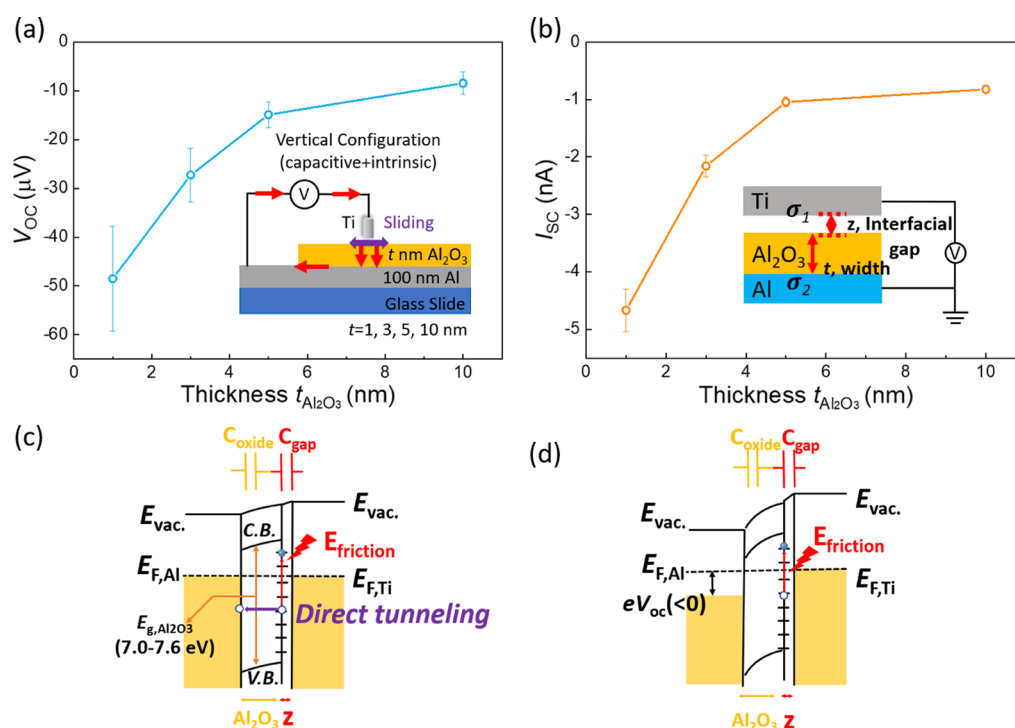
Figure 6. (a) Average V_{OC} output of the vertical structure with an increasing Al_2O_3 thickness $t_{Al2O3} = 1, 3, 5,$ and 10 nm; inset: schematic illustration of vertical configuration with $Ti/Al_2O_3/Al$ sliding contacts employing both the capacitive and intrinsic effects; (b) average I_{SC} versus the thickness of the Al_2O_3 layer t_{Al2O3}; inset: schematic illustration of the contact electrification process by the metal−oxide−metal system ($Ti/Al_2O_3/Al$). Energy band diagram of Al_2O_3 as the interfacial layer with a large band gap $E_{g, Al2O3}$ ∼7.0−7.6 eV under the (c) short-circuit condition and (d) open-circuit condition, where direct tunneling is the only possible mechanism for charge transport.

thick TiO_2 (Figure 4f), a completely different trend and clear trough region could be observed when the TiO_2 thickness reaches 100 and 200 nm, which indicates the involvement of F−N tunneling at high voltage. It can be seen that the trough region starts around $1/V = 0.25$ V^{-1} which corresponds to 4 V. However, the voltage generated by the sliding contact system is around 0.3−0.6 V under such thicknesses, which should be insufficient to trigger F−N tunneling, since the high interfacial thickness also makes direct tunneling impossible to occur. Therefore, a synergistic combination of trap-assisted SLSC, thermionic emission, and/or valence-band hole transport plays the dominant role under higher thicknesses of TiO_2 (100−200 nm).

To further investigate the $Al/TiO_2/Ti$ sliding contact systems, speed- (Figure 5a) and force- (Figure 5b) dependent V_{OC} and I_{SC} measurements have been carried out on the vertical configuration ($t_{TiO_2} = 100$ nm). A motor-driven testing system has been built to precisely control the applied force and relative sliding speed. As shown in Figure 5a, the V_{OC} increases from 32.92 to 126.78 mV as the sliding speed increases from 5 to 25 mm s^{-1} (under 0.1 N). On the other hand, J_{SC} in Figure 5a initially shows a similar tendency from 5−15 mm s^{-1} and then becomes saturated beyond 15 mm s^{-1}. Analogously, a clear J_{SC} output with positive correlation can be seen in Figure 5b under increasing force from 0.05−0.2 N. Such behaviors are in good accordance with eq 10. As the speed and force are increased, more intensive surface lattice distortion could be expected with a decreasing gap distance and contact area, which can result in the enhancement of the charge density and density of surface states. Additionally, such a feature of positive correlation could be attributed to the rise of mechanical energy input. In addition, it is worthy to point out that the V_{OC} output

as a function of increasing force (Figure 5b) reveals a slightly trim back, which may be due to the reduction of t_{TiO_2} resulting from tip indentation with accumulating applied local force/pressure (Figure 2a).

In order to further investigate the mechanism of tribovoltaic excitation, $Ti/Al_2O_3/Al$ sliding contact devices with the increasing thickness of Al_2O_3 have been fabricated via ALD and E-beam deposition on glass slides. Figure 6a shows the V_{OC} measured between the vertical configuration (schematic illustration shown in the inset figure) with the increasing thickness of Al_2O_3 ($t_{Al2O3} = 1, 3, 5,$ and 10 nm). Different from what has been observed with the TiO_2 system, a decrease in V_{OC} from −48.51 to −8.42 μV can be observed as the thickness of the Al_2O_3 layer increases from 1 to 10 nm, which is 4−5 orders of magnitude lower than with TiO_2 as the interfacial layer. The decreasing tendency of V_{OC} versus alumina thickness is an indication of a reduced charge density variation $\Delta\sigma$ when the alumina thickness increases (ΔV_{OC} in eq 9), which may be associated with the sub-band-gap excitation between the surface states as the only tribovoltaic excitation mechanism. The I_{SC} signal has also been measured as shown in Figure 6b. The inset figure shows the schematic illustration of the parallel model of the $Ti/Al_2O_3/Al$ junction with vertical configuration. Similar to the trend revealed by the V_{OC} output, it can be seen that the I_{SC} decreases from −4.67 to −0.82 nA as the thickness of the Al_2O_3 layer increases from 1 to 10 nm. The small DC output may be attributed to the wide band gap of Al_2O_3 (7.0−7.6 eV)[51] compared to that of TiO_2 (3.0−3.2 eV),[52,53] where direct tunneling is the only possible mechanism for charge transport (Figure 6c). In the meantime, as shown in Figure 6d, the reduction of the output voltage also accounts for the reduction of I_{SC}. This result indicates that an

optimal band gap may exist for enhanced tribovoltaic DC generation based on the semiconductor dynamic heterojunction.

CONCLUSIONS

In summary, by evaluating the DC output characteristics of MIM heterojunctions with different conducting pathways in vertical and horizontal configurations, the understanding of the fundamental roles of the interfacial layer (TiO$_2$) has been significantly advanced. In vertical configuration, V_{OC} shows a linear amplification effect as a function of the interfacial layer thickness, which is supported by a theoretical model based on the parallel capacitive effect. It is proposed that both the tribovoltaic effect generated by the Al/TiO$_2$ sliding contacts and the capacitive effect of the interfacial layer will contribute to the voltage generation in the vertical configuration. On the contrary, the produced voltage through horizontal configuration is only associated with the intrinsic effect. Meanwhile, J_{SC} shows an initial increasing trend and then a decreasing trend as t_{TiO_2} increases and reaches a peak value with the interfacial layer thickness at 20 nm, which is due to a competition between amplified voltage and increased resistance with increasing interfacial layer thickness, which implies that removing the oxide or a lower thickness of the oxide plays a vital role in the performance enhancement of DC generation under short-circuit conditions. The ionic passivation of thin TiO$_2$ (<20 nm) also facilitates the current transfer through the interface. Under such a scenario, thermionic emission/trap-assisted transport surpasses tunneling, becoming the dominating charge-transport mechanism as the interfacial layer thickness increases, whereas tunneling-based mechanisms are the main contributors for the DC output. These essential understandings provide new guidelines for optimizing energy harvesting performance for future dynamic DC generators.

ASSOCIATED CONTENT

Supporting Information

The Supporting Information is available free of charge at https://pubs.acs.org/doi/10.1021/acsami.1c22438.

Detailed AFM peak force topology images of TiO$_2$ and Al$_2$O$_3$ thin films; detailed AFM peak force topology images from multiple locations on the cross-sectional surface of Al probes; calculated R_g and R_a from various locations based on Figure S2; I−V characterizations of vertical configuration and horizontal configuration; I−V characteristics based on the F−N tunneling model, and $\ln(J/V^2)$ versus $1/V$ curves of vertical configuration and horizontal configuration (PDF)

AUTHOR INFORMATION

Corresponding Author

Jun Liu − *Department of Mechanical and Aerospace Engineering and RENEW (Research and Education in Energy, Environment and Water) Institute, University at Buffalo, The State University of New York, Buffalo, New York 14260, United States;* orcid.org/0000-0001-6951-8826; Email: jliu238@buffalo.edu

Authors

Matthew Benner − *Department of Mechanical and Aerospace Engineering, University at Buffalo, The State University of New York, Buffalo, New York 14260, United States*

Ruizhe Yang − *Department of Mechanical and Aerospace Engineering, University at Buffalo, The State University of New York, Buffalo, New York 14260, United States*

Leqi Lin − *Department of Mechanical and Aerospace Engineering, University at Buffalo, The State University of New York, Buffalo, New York 14260, United States*

Maomao Liu − *Department of Electrical Engineering, University at Buffalo, The State University of New York, Buffalo, New York 14260, United States*

Huamin Li − *Department of Electrical Engineering, University at Buffalo, The State University of New York, Buffalo, New York 14260, United States;* orcid.org/0000-0001-7093-4835

Complete contact information is available at:
https://pubs.acs.org/10.1021/acsami.1c22438

Author Contributions

M.B. and R.Y. contributed equally to this work. J.L. conceived the idea of the work. M.B., R.Y., and J.L. designed and conducted the experiments. M.L. and H.L. analyzed the I−V measurements. The manuscript was written through contributions of all authors. All authors have given approval to the final version of the manuscript.

Notes

The authors declare no competing financial interest.

REFERENCES

(1) Wu, C.; Wang, A. C.; Ding, W.; Guo, H.; Wang, Z. L. Triboelectric Nanogenerator: A Foundation of the Energy for the New Era. *Adv. Energy Mater.* **2019**, *9*, 1802906.

(2) Wang, S.; Lin, L.; Wang, Z. L. Triboelectric Nanogenerators as Self-Powered Active Sensors. *Nano Energy* **2015**, *11*, 436−462.

(3) Wang, Z. L.; Wang, A. C. On the Origin of Contact-Electrification. *Mater. Today* **2019**, *30*, 34−51.

(4) Wang, Z. L. Triboelectric Nanogenerators as New Energy Technology for Self-Powered Systems and as Active Mechanical and Chemical Sensors. *ACS Nano* **2013**, *7*, 9533−9557.

(5) Liu, J.; Goswami, A.; Jiang, K.; Khan, F.; Kim, S.; McGee, R.; Li, Z.; Hu, Z.; Lee, J.; Thundat, T. Direct-Current Triboelectricity Generation By a Sliding Schottky Nanocontact on MoS$_2$ Multilayers. *Nat. Nanotechnol.* **2018**, *13*, 112−116.

(6) Yang, R.; Xu, R.; Dou, W.; Benner, M.; Zhang, Q.; Liu, J. Semiconductor-Based Dynamic Heterojunctions as an Emerging Strategy for High Direct-Current Mechanical Energy Harvesting. *Nano Energy* **2021**, *83*, 105849.

(7) Liu, J.; Zhang, Y.; Chen, J.; Bao, R.; Jiang, K.; Khan, F.; Goswami, A.; Li, Z.; Liu, F.; Feng, K.; Luo, J.; Thundat, T. Separation and Quantum Tunneling of Photo-generated Carriers Using a Tribo-Induced Field. *Matter* **2019**, *1*, 650−660.

(8) Liu, J.; Liu, F.; Bao, R.; Jiang, K.; Khan, F.; Li, Z.; Peng, H.; Chen, J.; Alodhayb, A.; Thundat, T. Scaled-up Direct-Current Generation in MoS$_2$ Multilayer-Based Moving Heterojunctions. *ACS Appl. Mater. Interfaces* **2019**, *11*, 35404−35409.

(9) Lu, Y.; Feng, S.; Shen, R.; Xu, Y.; Hao, Z.; Yan, Y.; Zheng, H.; Yu, X.; Gao, Q.; Zhang, P.; Lin, S. Tunable Dynamic Black Phosphorus/Insulator/Si Heterojunction Direct-Current Generator Based on the Hot Electron Transport. *Research* **2019**, *2019*, 1.

(10) Huang, X.; Xiang, X.; Nie, J.; Peng, D.; Yang, F.; Wu, Z.; Jiang, H.; Xu, Z.; Zheng, Q. Microscale Schottky Superlubric Generator

With High Direct-Current Density and Ultralong Life. *Nat. Commun.* **2021**, *12*, 2268.

(11) Chen, J.; He, P.; Huang, T.; Zhang, D.; Wang, G.; Yang, S.; Xie, X.; Ding, G. Boosting Carrier Transfer at Flexible Schottky Junctions with Moisture: A Strategy for High-Performance Wearable Direct-Current Nanogenerators. *Nano Energy* **2021**, *90*, 106593.

(12) Ma, C.; Kim, B.; Kim, S.-W.; Park, N.-G. Dynamic Halide Perovskite Heterojunction Generates Direct Current. *Energy Environ. Sci.* **2021**, *14*, 374−381.

(13) Hao, Z.; Jiang, T.; Lu, Y.; Feng, S.; Shen, R.; Yao, T.; Yan, Y.; Yang, Y.; Lu, Y.; Lin, S. Co-harvesting Light and Mechanical Energy Based on Dynamic Metal/Perovskite Schottky Junction. *Matter* **2019**, *1*, 639−649.

(14) Shao, H.; Fang, J.; Wang, H.; Dai, L.; Lin, T. Polymer-Metal Schottky Contact with Direct-Current Outputs. *Adv. Mater.* **2016**, *28*, 1461−1466.

(15) Meng, J.; Guo, Z. H.; Pan, C.; Wang, L.; Chang, C.; Li, L.; Pu, X.; Wang, Z. L. Flexible Textile Direct-Current Generator Based on the Tribovoltaic Effect at Dynamic Metal-Semiconducting Polymer Interfaces. *ACS Energy Lett.* **2021**, *6*, 2442−2450.

(16) Yang, R.; Benner, M.; Guo, Z.; Zhou, C.; Liu, J. High-Performance Flexible Schottky DC Generator via Metal/Conducting Polymer Sliding Contacts. *Adv. Funct. Mater.* **2021**, *31*, 2103132.

(17) You, Z.; Wang, S.; Li, Z.; Zou, Y.; Lu, T.; Wang, F.; Hu, B.; Wang, X.; Li, L.; Fang, W.; Liu, Y. High Current Output Direct-Current Triboelectric Nanogenerator Based on Organic Semi-conductor Heterojunction. *Nano Energy* **2022**, *91*, 106667.

(18) Ying, S.; Zhang, J.-H.; Yan, K.; Xin, M.; Zhang, J.; Li, S.; Liang, J.-G.; Shi, Y.; Pan, L. Self-Powered Direct-current Type Pressure Sensor by Polypyrrole/Metal Schottky Junction. *J. Phys. D: Appl. Phys.* **2021**, *54*, 424008.

(19) Liu, J.; Cheikh, M. I.; Bao, R.; Peng, H.; Liu, F.; Li, Z.; Jiang, K.; Chen, J.; Thundat, T. Tribo-Tunneling DC Generator with Carbon Aerogel/Silicon Multi-Nanocontacts. *Adv. Electron. Mater.* **2019**, *5*, 1900464.

(20) Liu, J.; Miao, M.; Jiang, K.; Khan, F.; Goswami, A.; McGee, R.; Li, Z.; Nguyen, L.; Hu, Z.; Lee, J.; Cadien, K.; Thundat, T. Sustained electron tunneling at unbiased metal-insulator-semiconductor tribo-electric contacts. *Nano Energy* **2018**, *48*, 320−326.

(21) Zhang, Z.; He, T.; Zhao, J.; Liu, G.; Wang, Z. L.; Zhang, C. Tribo-Thermoelectric and Tribovoltaic Coupling Effect at Metal-Semiconductor Interface. *Mater. Today Phys.* **2021**, *16*, 100295.

(22) Lin, S.; Lu, Y.; Feng, S.; Hao, Z.; Yan, Y. A High Current Density Direct-Current Generator Based on a Moving van der Waals Schottky Diode. *Adv. Mater.* **2019**, *31*, 1804398.

(23) Wang, Y.; Zhang, G.; Wu, H.; Sun, B. Simultaneously Harvesting Friction and Solar Energy via Organic/Silicon Hetero-junction with High Direct-Current Generation. *Adv. Energy Mater.* **2021**, *11*, 2100578.

(24) Lin, S.; Xu, L.; Chi Wang, A.; Wang, Z. L. Quantifying Electron-Transfer in Liquid-Solid Contact Electrification and the Formation of Electric Double-Layer. *Nat. Commun.* **2020**, *11*, 399.

(25) Lu, Y.; Yan, Y.; Yu, X.; Zhou, X.; Feng, S.; Xu, C.; Zheng, H.; Yang, Z.; Li, L.; Liu, K.; Lin, S. Polarized Water Driven Dynamic PN Junction-Based Direct-Current Generator. *Research* **2021**, *2021*, 1.

(26) Lin, S.; Chen, X.; Wang, Z. L. The Tribovoltaic Effect and Electron Transfer at a Liquid-Semiconductor Interface. *Nano Energy* **2020**, *76*, 105070.

(27) Zhang, Z.; Jiang, D.; Zhao, J.; Liu, G.; Bu, T.; Zhang, C.; Wang, Z. L. Tribovoltaic Effect on Metal-Semiconductor Interface for Direct-Current Low-Impedance Triboelectric Nanogenerators. *Adv. Energy Mater.* **2020**, *10*, 1903713.

(28) Zheng, M.; Lin, S.; Xu, L.; Zhu, L.; Wang, Z. L. Scanning Probing of the Tribovoltaic Effect at the Sliding Interface of Two Semiconductors. *Adv. Mater.* **2020**, *32*, 2000928.

(29) Nie, J.; Ren, Z.; Xu, L.; Lin, S.; Zhan, F.; Chen, X.; Wang, Z. L. Probing Contact-Electrification-Induced Electron and Ion Transfers at a Liquid-Solid Interface. *Adv. Mater.* **2020**, *32*, 1905696.

(30) Liu, J.; Jiang, K.; Nguyen, L.; Li, Z.; Thundat, T. Interfacial Friction-Induced Electronic Excitation Mechanism for Tribo-Tunnel-ing Current Generation. *Mater. Horiz.* **2019**, *6*, 1020−1026.

(31) Cui, S.; Zhou, L.; Liu, D.; Li, S.; Liu, L.; Chen, S.; Zhao, Z.; Yuan, W.; Wang, Z. L.; Wang, J. Improving Performance of Triboelectric Nanogenerators by Dielectric Enhancement Effect. *Matter* **2021**, *5*, 1−14.

(32) Lu, Y.; Hao, Z.; Feng, S.; Shen, R.; Yan, Y.; Lin, S. Direct-Current Generator Based on Dynamic PN Junctions with the Designed Voltage Output. *iScience* **2019**, *22*, 58−69.

(33) Chiu, F.-C. A Review on Conduction Mechanisms in Dielectric Films. *Adv. Mater. Sci. Eng.* **2014**, *2014*, 578168.

(34) Zhou, Y. S.; Wang, S.; Yang, Y.; Zhu, G.; Niu, S.; Lin, Z.-H.; Liu, Y.; Wang, Z. L. Manipulating Nanoscale Contact Electrification by an Applied Electric Field. *Nano Lett.* **2014**, *14*, 1567−1572.

(35) Lenzlinger, M.; Snow, E. H. Fowler-Nordheim Tunneling into Thermally Grown SiO_2. *J. Appl. Phys.* **1969**, *40*, 278−283.

(36) Maserjian, J.; Zamani, N. Behavior of the Si/SiO_2 Interface Observed by Fowler-Nordheim Tunneling. *J. Appl. Phys.* **1982**, *53*, 559−567.

(37) Iqbal, M. Z.; Faisal, M. M. Fowler-Nordheim Tunneling Characteristics of Graphene/hBN/Metal Heterojunctions. *J. Appl. Phys.* **2019**, *125*, 084902.

(38) Murphy, E. L.; Good, R. H. Thermionic Emission, Field Emission, and the Transition Region. *Phys. Rev.* **1956**, *102*, 1464−1473.

(39) Herring, C.; Nichols, M. H. Thermionic Emission. *Rev. Mod. Phys.* **1949**, *21*, 185−270.

(40) Nienhaus, H.; Glass, S. Probing the Distribution of Hot Charge Carriers Generated in Mg Surfaces by Oxidation. *Surf. Sci.* **2006**, *600*, 4285−4289.

(41) Wang, G.; Li, J.; Lv, K.; Zhang, W.; Ding, X.; Yang, G.; Liu, X.; Jiang, X. Surface thermal oxidation on titanium implants to enhance osteogenic activity and in vivo osseointegration. *Sci. Rep.* **2016**, *6*, 31769.

(42) Lowell, J.; Rose-Innes, A. C. Contact Electrification. *Adv. Phys.* **1980**, *29*, 947−1023.

(43) Lowell, J. Tunnelling Between Metals and Insulators and its Role in Contact Electrification. *J. Phys. D: Appl. Phys.* **1979**, *12*, 1541−1554.

(44) Antony, A. C.; Thelen, D.; Zhelev, N.; Adib, K.; Manley, R. G. Electronic Charge Transfer During Metal/SiO_2 Contact: Insight from Density Functional Theory. *J. Appl. Phys.* **2021**, *129*, 065304.

(45) Xu, R.; Zhang, Q.; Wang, J. Y.; Liu, D.; Wang, J.; Wang, Z. L. Direct Current Triboelectric Cell by Sliding an n-type Semiconductor on a p-type Semiconductor. *Nano Energy* **2019**, *66*, 104185.

(46) Zhang, J.; Rogers, F. J. M.; Darwish, N.; Gonçales, V. R.; Vogel, Y. B.; Wang, F.; Gooding, J. J.; Peiris, M. C. R.; Jia, G.; Veder, J.-P.; Coote, M. L.; Ciampi, S. Electrochemistry on Tribocharged Polymers Is Governed by the Stability of Surface Charges Rather than Charging Magnitude. *J. Am. Chem. Soc.* **2019**, *141*, 5863−5870.

(47) Ferrie, S.; Darwish, N.; Gooding, J. J.; Ciampi, S. Harnessing Silicon Facet-Dependent Conductivity to Enhance the Direct-Current Produced by a Sliding Schottky Diode Triboelectric Nanogenerator. *Nano Energy* **2020**, *78*, 105210.

(48) Lin, Y.; Kapadia, R.; Yang, J.; Zheng, M.; Chen, K.; Hettick, M.; Yin, X.; Battaglia, C.; Sharp, I. D.; Ager, J. W.; Javey, A. Role of TiO_2 Surface Passivation on Improving the Performance of p-InP Photocathodes. *J. Phys. Chem. C* **2015**, *119*, 2308−2313.

(49) Chen, T.-C.; Yang, T.-C.; Cheng, H.-E.; Yu, I.-S.; Yang, Z.-P. Single Material TiO_2 Thin Film by Atomic Layer Deposition for Antireflection and Surface Passivation Applications on p-type c-Si. *Appl. Surf. Sci.* **2018**, *451*, 121−127.

(50) Kwan, C.-P.; Street, M.; Mahmood, A.; Echtenkamp, W.; Randle, M.; He, K.; Nathawat, J.; Arabchigavkani, N.; Barut, B.; Yin, S.; Dixit, R.; Singisetti, U.; Binek, C.; Bird, J. P. Space-Charge Limited Conduction in Epitaxial Chromia Films Grown on Elemental and Oxide-Based Metallic Substrates. *AIP Adv.* **2019**, *9*, 055018.

(51) Filatova, E. O.; Konashuk, A. S. Interpretation of the Changing the Band Gap of Al_2O_3 Depending on Its Crystalline Form: Connection with Different Local Symmetries. *J. Phys. Chem. C* **2015**, *119*, 20755−20761.

(52) Dette, C.; Pérez-Osorio, M. A.; Kley, C. S.; Punke, P.; Patrick, C. E.; Jacobson, P.; Giustino, F.; Jung, S. J.; Kern, K. TiO_2 Anatase with a Bandgap in the Visible Region. *Nano Lett.* **2014**, *14*, 6533−6538.

(53) Reyes-Coronado, D.; Rodríguez-Gattorno, G.; Espinosa-Pesqueira, M. E.; Cab, C.; de Coss, R.; Oskam, G. Phase-Pure TiO_2 Nanoparticles: Anatase, Brookite and Rutile. *Nanotechnology* **2008**, *19*, 145605.